Computational Materials Science 216 (2023) 111875

Contents lists available at ScienceDirect

Computational Materials Science

journal homepage: www.elsevier.com/locate/commatsci

Letter

Examining solid-state sintering of AlCoCrFeNi multi-principal element alloy by molecular simulations

Praveen Sreeramagiri [a], Prince Sharma [a,b], Chayan Das [a], Ganesh Balasubramanian [a,b,*]

[a] Department of Mechanical Engineering and Mechanics
[b] Institute for Functional Materials and Devices Lehigh University, 19, Memorial Drive West, Bethlehem, PA 18015, USA

ARTICLE INFO

Keywords:
Solid-state sintering
Multi-principal element alloys
Molecular dynamics
Phase transformation

ABSTRACT

With the emergence of solid-state sintering techniques for metal additive manufacturing of multicomponent alloys, understanding the fundamental sintering mechanisms is vital for effective process control. Here, we employ molecular dynamics simulations to investigate the mechanisms involved during solid-state sintering of AlCoCrFeNi multi-principal element alloy. Our results reveal that the cross migration of atoms between the surface of powder particles promotes neck growth while minimizing the surface free energy. This phenomenon is mediated by a transition from BCC to amorphous phase resembling a pre-melt and assisting in the densification as a function of temperature. Stress–strain analysis on the alloy single crystal at room temperature suggests that permanent plastic deformation occurs with a gradual phase change to FCC predicting a tensile strength of ~ 1547 MPa at the onset of yield and a peak stress of 2267 MPa.

1. Solid-state additive manufacturing techniques

Additive manufacturing (AM) of multi-principal element alloys (MPEAs) has witnessed a significant growth in the past few years owing to the notable (and high-throughput) capabilities of such fabrication platforms, and the resultant mechanical properties of the alloys [1–5]. MPEAs are concentrated solid-solutions, distinct from conventional alloys, and their synthesis using AM often constitutes a twofold process, *i.e.,* alloy design and component fabrication. Amongst AM methods, directed energy deposition (DED) is primarily centered around alloy development [6] with minimal emphasis on component fabrication, predominantly due to the poor surface finish resulting from relatively higher layer heights. On the contrary, the low layer heights in powder bed fusion (PBF) produces excellent surface finish and requires minimal post-processing ideal for component fabrication [7].

While these two techniques employ high energy densities to synthesize components, recent advancements in metal AM promote hybrid processes (*viz.,* binder jetting, fused filament fabrication) driven by solid-state sintering techniques. The latter are dissimilar to conventional AM approaches in that the material never reaches its melting point ensuing in a different synthesis mechanism. The sintering-based AM processes comprise of printing followed by evaporation of the binder (green part) and sintering/densification to fabricate a component [8,9]. Though the printing and evaporation steps are analogous to any other non-metal AM, sintering a material by itself is unique; hence, understanding the underlying mechanisms during the processing will offer insights on the resultant microstructural phases and the mechanical properties of the MPEAs [10]. Sintering of powder particles by melting and solidification for conventional alloys has been reported previously [10–14], but literature on the solid-state sintering for additive manufacturing of MPEAs are sparse [15–18]. Here, we employ atomistic simulations to interrogate the fundamental mechanisms during solid state sintering by isobaric heating of the equiatomic AlCoCrFeNi MPEA, and analyze the resulting microstructures and mechanical properties. In addition, our works sheds light on choosing the right temperatures to anneal the MPEA to achieve high density parts during sintering.

2. Predictive modeling

2.1. Potential Validation:

We initiate our study with the search for appropriate potentials that can describe the interaction between constituent elements. Of the available embedded atom method (EAM) potentials for this MPEA family ($Al_xCoCrFeNi$) [19–21], we choose the methods outlined by Fourmont et. al. [18] and Sreeramagiri et. al. [21] for their ability to

* Corresponding author at: 19 Memorial Drive West, Lehigh University, Bethlehem, PA 18015.
E-mail address: bganesh@lehigh.edu (G. Balasubramanian).

https://doi.org/10.1016/j.commatsci.2022.111875
Received 26 March 2022; Received in revised form 12 October 2022; Accepted 16 October 2022
Available online 23 October 2022

accurately predict the BCC phase in equiatomic condition [21–24]. The parameters for potentials are adopted from Zhou et al. [23] for Al, Co, Fe, Ni, and Lin et al. [24] for Cr; which are fed to the LAMMPS in-built combinatorial potential development tool to collectively create ten cross-interactions between the constituent elements in the alloy system using EAM method [25,26].

To assert our choice of potentials, we perform a validation study to assess the melting point upon heating and the phases realized upon cooling the AlCoCrFeNi MPEA. We estimate the phase formation, melting and solidification temperatures of the alloy, as reported elsewhere [21], to validate the potentials employed in the simulations to predict the sintering temperature of the AlCoCrFeNi MPEA. We acknowledge that the sphere method using the Gibbs-Thompson effect could possibly offer more accurate estimates, but it is not the goal of the current study. Though we perform three simulations with varying atom counts (~10,000; 30,000 and 88,000 atoms) to estimate the melting point (to eliminate the size effects on melting point estimates), we utilize only one of them (~30,000) to further cool the MPEA to efficiently utilize the computational resources. Atoms of all the simulation domains are randomly distributed with candidate elements in a BCC crystal lattice (widely accepted for this material system and our earlier experiments [27]) with a lattice parameter of 2.86 Å. The simulations are performed in the LAMMPS package [28] and we use OVITO [29] for visualizations. Among the various sizes, we stress our results from the simulation box containing ~ 30,000 atoms with a domain size of 70 Å × 70 Å × 70 Å as we see no difference in melting points with varying sizes. The melting point estimates of the other two box sizes are presented as supplementary information.

The simulation box is energy minimized using the conjugate gradient method with force and energy tolerances of 10^{-15} eV/Å and 10^{-15} eV, respectively. The simulation domain is initiated at 300 K and heated to 2500 K at an arbitrary heating rate and subsequently cooled to 300 K at a cooling rate of 4.5×10^{8} K/s. Here, we choose the cooling rate that predicts a crystal post solidification as opposed to amorphous. We use a time step of 0.08 ps, optimized to accelerate the computation time with available resources for cooling the bulk alloy. Fig. 1 (a) and Figure S1 (in the supplementary information) display the density as a function of temperature during the heating and solidification of AlCoCrFeNi MPEA. As can be evinced, our potentials predict a melting point of ~ 1735 K, which is in well agreement with the literature for the current system with a difference of < 100 K attributed to the superheating effects and artifacts from simulations as explained in the literature [21]. However, we conjuncture the low solidification temperature of ~ 960 K is a result of homogenous nucleation and under cooling effects [21,30]. Upon cooling, we note a BCC crystal as visualized from polyhedral template matching (PTM), validating the applicability of potentials for the current material system.

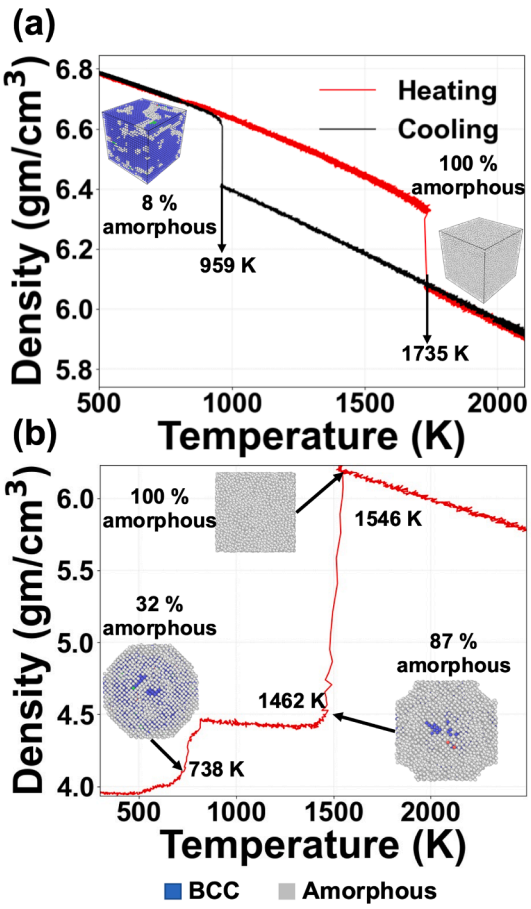

Fig. 1. (a) Density variation with temperature during heating and cooling of the MPEA suggests a transition of phase from BCC to amorphous at 1735 K when heating, with our predictions in good agreement with the literature. The cooling curve suggests a solidification temperature of ~ 960 K significantly lower than the equilibrium crystallization temperature, which is attributed to the undercooling and homogenous nucleation. (b) Density variation with temperature when melting a powder particle suggests the initiation of melting at ~ 1460 K and ending at ~ 1546 K. A relatively lower melting point of the powder particle is attributed to the lower surface energy of the sphere compared to the cube.

2.2. AlCoCrFeNi nano-particles

Similar to the bulk material, we create an AlCoCrFeNi nano powder particle of radius 1.7 nm in a BCC lattice with the constituent elements randomly distributed in near equiatomic composition with a lattice parameter of 2.86 Å [21]. This particle is energy minimized using the conjugate gradient method with force and energy tolerances of 10^{-15} eV/Å and 10^{-15} eV, respectively. To understand the differences in melting mechanisms between bulk and powder forms of the MPEA, we subject the powder particle to an increasing temperature from 300 K to 2500 K and capture details like density and phase formation at various instances as presented in Fig. 1 (b). This enables us to determine the sintering temperature such that we do not exceed the melting point of the material in powder form.

Next, 3 additional replications of the powder particle are arranged ~ 8 Å apart from each other, with periodic boundary conditions imposed along all three directions as illustrated in Fig. 2(a). The selected distance facilitates a sufficient gap between the particles such that none of them are in contact with each other when initializing the simulation box. To eliminate artifacts associated with the model construction, the simulation domain incorporating four powder particles is energy minimized enforcing the same conditions as stated above. Post minimization, the particles in the system assume a stable BCC crystal structure as verified from the polyhedral template matching (PTM) [31] as displayed in Fig. 2 (b). The system is then gradually heated to 1400 K with intermediate equilibration at 500, 800, 1000, 1200 and 1400 K, under the isothermal-isobaric (NPT) ensemble using a Nose-Hoover thermostat with a coupling time of 1 ps and a barostat constraining the pressure at 0 bar every 1000 timesteps. A heating rate of 0.6 K/ps is employed, followed by equilibration for 100,000 timesteps at each temperature milestone. The procedure mimics thermal annealing of the green body free from binder, ready to be sintered with no local heating or reactions involved. Upon sintering/densification, the alloy is cooled to 300 K with a cooling rate of 1.1 K/ps for microstructural characterization. We estimate the change in the surface energy during sintering using density functional theory (DFT) calculations, as elaborated in the supplementary information. Additionally, we examine the stress evolution in the sintered alloy (aggregated nano-particles analogous to a bulk material after sintering) cooled to 300 K with an applied tensile strain rate of 10^{-9} /s. A timestep of 1 fs is used for all the sintering simulations.

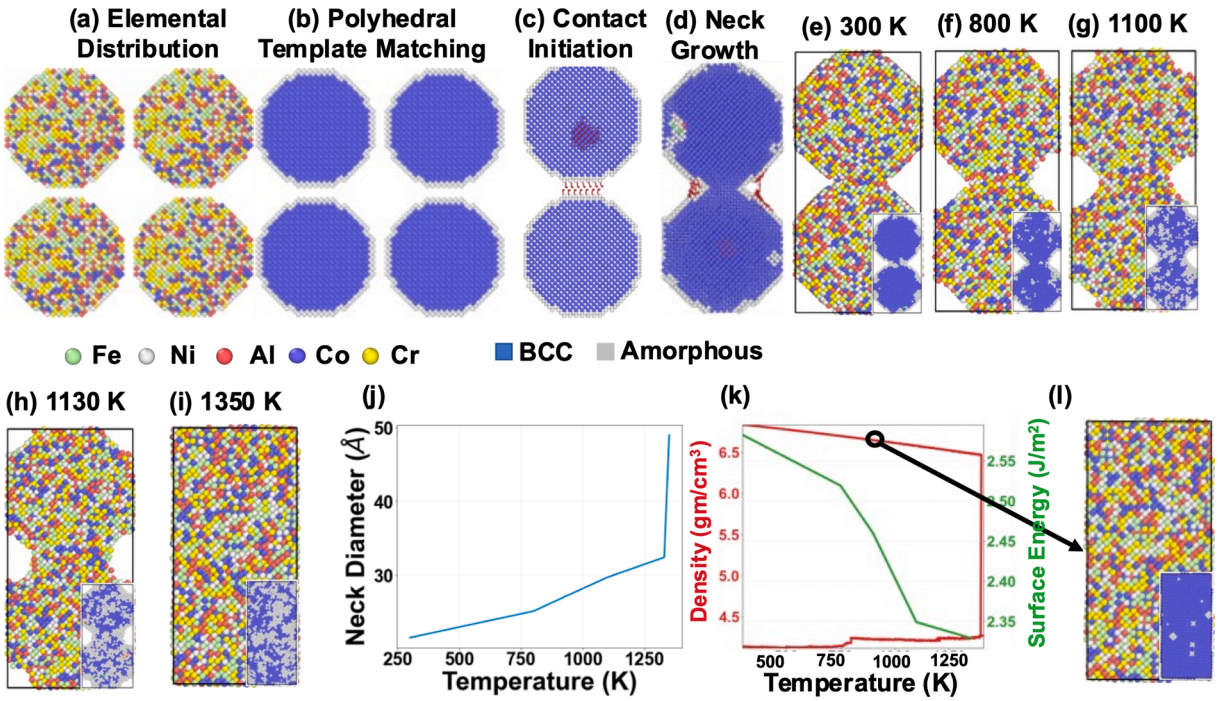

Fig. 2. (a) Four nanoscale particles of the equiatomic AlCoCrFeNi MPEA are situated in the simulation box with ~ 8 Å spacing between them. (b) Polyhedral template matching (PTM) of the particle cross-section verifies a single-phase BCC lattice with amorphous phase at the particle boundaries. (c) Trajectories of representative atoms on the surface and in the core of the particles, with the former facilitating contact between adjacent particles. (d) Atoms on the surface of the MPEA particles penetrate the surface of the neighboring powder particles promoting neck growth. (e-i) Snapshots of the atom distributions at various temperatures during the sintering validates the neck growth that is driven by phase transition from BCC to amorphous and re-crystallization at the interface, (j) The increase in neck diameter with increasing temperatures is indicative of the densification of the alloy. (k) The density profile recorded during sintering reveals complete densification of the MPEA at ~ 800 K, and (l) with a random distribution of the constituent elements in a BCC solid-solution phase. In addition, the reducing surface energy signifies the elimination of free surface area due to bond growth,

3. Results and discussion

Fig. 1 (a) and (b) display the difference in behaviors of bulk material relative to the powder particle, both composed of the MPEA. The simulation domain for the bulk material is cuboidal; the powder particle is created by removing excess atoms within the cube to render a sphere as a remainder. Thus, the powder particle exhibits a low density of ~ 4 gm/cm^3 at 300 K, as the volume of a cube is considered with vacuum surrounding the sphere. This associated low density and minimum surface energy of the sphere relative to the cube enable the insinuation of melting at a relatively low temperature of ~ 1462 K for the powder particle (in comparison to the bulk material *viz.,* 1735 K). In addition, we note a slight density change at ~ 738 K, which is attributed to the expansion of powder particle to the faces of the cube simulation domain along with a gradual change to amorphous phase as revealed by the PTM. Thus, we choose an annealing temperature of 1400 K, which is well below the melting point of powder particle for our solid-state sintering simulations.

The strong attraction between adjacent powder particles, dictated by the interatomic potentials employed [12], facilitates the incubation of contact between them, even before thermal energy is imposed on the simulation domain through the temperature initiation at 300 K (Fig. 2 (c-d)). During contact initiation, the atoms on the surface of the one powder particle in proximity to the surface atoms on the other particles move towards each other (Fig. 2(c)) establishing the contact. Upon contact initiation, the atoms on the surfaces of these particles migrate and penetrate the surfaces of the neighboring powder particles to promote densification. This process minimizes the surface free energy, as presented in Fig. 2(d) and (k). Conversely, atoms at the core of these particles remain predominantly stationary in a quasi-static phase. Further densification of alloy is driven by the inter-diffusion of surface atoms of the alloys due to an increase in temperatures (Fig. 2 (e-i)), resulting in neck growth (Fig. 2 (j)). Table 1 lists the neck diameter and phase constitution derived from a polyhedral template matching (PTM) of snapshots sampled across different temperatures during the simulations. The results suggest a transformation from BCC to an amorphous phase with increasing temperatures near the neck region, exemplifying a pre-melt layer followed by re-crystallization [11]. Subsequently, a steep increase in neck diameter witnessed at ~ 1397 K (~77 % of melting temperature) symbolizes the cessation of densification, whence the atoms assume an amorphous microstructure (up to 82 % of the crystallographic phase composition) due to the accumulated free energy. Incidentally, the steep gradient in the alloy density that is recorded around the same temperature asserts this phenomenon (Fig. 2 (k)) [11,12,15–17,32]. Conversely, the surface energy, listed in Table 2, reduces with increasing temperatures signifying the loss of free surfaces during sintering. This loss is attributed to the contact initiation and bond growth between powder particles. We acknowledge that atomistic misorientations, vacancies, grain boundary impurities, can contribute to an offset in the predicted surface energies; within the scope for the current study, we interrogate the effects attributed to the bond formations and growth. Prior to sintering, powder particles exhibit dangling bonds at the free surfaces, whose interactions with atoms are responsible for the high initial surface energy. On contact followed by heating, the

Table 1
Neck diameter and phase constitution as a function of temperature during the solid-state sintering of AlCoCrFeNi multi-principal element alloy.

Temperature (K)	0	300	800	1100	1330	1350
Neck diameter (Å)	8	21.5	25.1	29.7	32.4	49
BCC Phase Fraction (%)	77.9	75.7	69	50	32.2	37.1
Amorphous Phase Fraction (%)	22	23.8	59	81.5	80.8	18.4

Table 2
Surface energies during sintering at different temperatures as estimated from the DFT calculations. The predictions indicate that surface energies reduce with increasing temperatures.

Temperature (K)	Surface Energy/Area (J/m^2)
300	2.582
750	2.519
900	2.460
1100	2.349
1350	2.329

dangling bonds of one powder particle contact with those of the adjacent particle, resulting in densification and reduced free surfaces and the surface energy. Our results are in close agreement with the literature pertaining to conventional BCC metals (e.g., tungsten [11]), suggesting that sintering in the complex MPEA is assisted by the formation and growth of the neck while promoting densification and reducing surface energy with increasing temperatures [11,17,33–35]. On cooling the MPEA, a gradual phase transformation to BCC is noted with a homogenous elemental distribution as illustrated in Fig. 2 (l) for ~ 800 K.

To understand the densification kinetics, we evaluate the mean squared displacement (MSD) of atoms occupying the interfacial zones between the powder particles (Fig. 3 (a)). We consider the molar average of MSD evaluated over atoms of all the constituent elements at the interface to understand the interfacial diffusion. The interfacial atoms are identified at each step by capturing the atoms at a fixed location between the two powder particles before every equilibration step. Fig. 3 reveals no significant movement of interfacial atoms other than a random noise below 1400 K. We attribute this behavior to the cessation of neck growth during heating and equilibration at respective temperatures, seizing the movement of atoms in solid state at respective temperatures. This is a consequence of initiating MSD evaluation post equilibration to ensure the stability of results. Thus, we conjuncture that the neck growth concluded before the initiation of MSD evaluation, and hence no meaningful results can be extracted out of MSD when the temperature is < 1200 K. However, the noise displayed in the MSD profiles is associated with the diffusion of atoms within the vacancies of the crystal lattice [36,37]. Nevertheless, the continually increasing MSD exhibited at 1400 K is attributed to the transformation of the crystal, to amorphous phase embodying the dynamics in the pre-melt (as supported by the PTM) [10,11].

Fig. 4 presents the stress evolution in the alloy under an applied tensile strain, post sintering and subsequent cooling to room temperature at 300 K. The alloy produces a yield stress of 1547 MPa at a strain of ~ 2.7 %. Dislocation analysis during the tensile testing advocates that the deformation until the yield point is assisted by ½ ⟨1 1 1⟩ type dislocations (Fig. 4 (b)), which is the dominant dislocation type in BCC lattices [38]. Straining the alloy further induces a permanent plastic deformation (yielding) mediated by a phase transition to FCC, with ~ 0.6 % phase fraction realized at the onset of yield (Fig. 4 (c)). Examining the dislocation behavior at the onset of yield confirms the phase transition mechanism revealing the formation of ⟨1 1 0⟩ type dislocations (dominant dislocation type in FCC lattice) with a length of ~ 5 Å. This phenomenon is followed by a gradual increase of FCC with ~ 3 % phase composition noted at the peak stress of 2267 MPa at a strain of 5.6 %. Further loading the alloy promotes a gradual increase of the FCC phase fraction rendering the alloy to be soft and ductile as recognized by the reducing flow stress in Fig. 4 (a). We report relatively high yield and peak stresses post sintering due to the single crystal nature of the simulated MPEA. Our results agree with prior reports suggesting that the material under solid-state sintering behaves similar to the equilibrated structures with no melting involved [21].

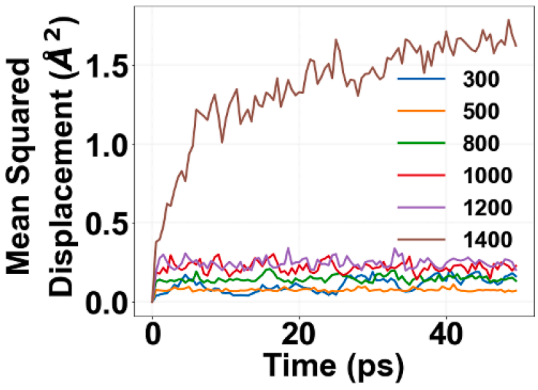

Fig. 3. Mean squared displacement (MSD) of the interfacial atoms during the solid-state sintering of AlCoCrFeNi MPEA. Molar averaged MSD of all the atoms at the interface of two powder particles evaluated across a temperature range reveals faster diffusion with increasing temperatures. However, results suggest no movement of atoms as a consequence of the cessation of neck growth even before the evaluation of MSD due to constant heating and equilibration at respective temperatures.

Our results suggest that MPEAs with high melting points can be fabricated at lower temperatures using sintering while retaining the mechanical properties and enable an accelerated design of new MPEAs. However, concerns remain in terms of the detrimental phases (σ, δ, etc.) that can nucleate during prolonged exposures to such high temperatures and must be accounted for in the materials processing. In addition, the methodology presented herein can be effectively used to identify the sintering temperatures for applications in powder metallurgy and additive manufacturing.

4. Conclusion

In summary, we simulate the solid-state sintering of the AlCoCrFeNi MPEA to understand the corresponding phase evolution and the resultant structural properties. We start with a systematic approach by validating the potentials used in our simulation. Further, we estimate the melting point of bulk BCC AlCoCrFeNi MPEA followed by subsequent cooling at 4.5×10^8 K/s. Melting and cooling the MPEA reveals a melting point of ~ 1735 K with close agreement to the literature. However, we evince a significantly lower crystallization temperature of ~ 960 K due to the undercooling effects. A comparison of melting from bulk to powder particle reveals a melting temperature difference of ~ 270 K evinced at ~ 1462 K due to the low surface energy of the powder particle relative to the bulk metal. Our sintering simulation encompasses four nanoscale powder particles that exhibit strong attraction, enabling contact between them even before temperature initiation at 300 K. Densification in this alloy is mediated by the cross migration of atoms between the surfaces of powder particles, reducing the surface free energy due to the formation and growth of new bonds between powder particles, promoting neck growth as a function of temperature (until ~ 1300 K); the atoms in the core of powder particle remain almost stationary or quasi-static in a BCC crystal. Increasing temperature further induces a phase change from BCC to amorphous (with ~ 82 % crystallographic phase constitution) at ~ 1397 K (~77 % of melting temperature) corroborating densification, which upon cooling reverts the crystal to a BCC phase at ~ 800 K. MSD results from our simulations reveal no movement of atoms suggesting the densification is ceased before its evaluation during heating and equilibration at the respective temperatures. Subsequently, mobility in the alloy is driven by vacancy diffusion of atoms within the particles. Stress–strain evolution of the sintered alloy reveals yield stress of 1547 MPa at a tensile strain of 2.7 %. We find that plastic deformation in this MPEA is mediated by a phase change from BCC to FCC, which is substantiated by the PTM and from the dislocation analysis.

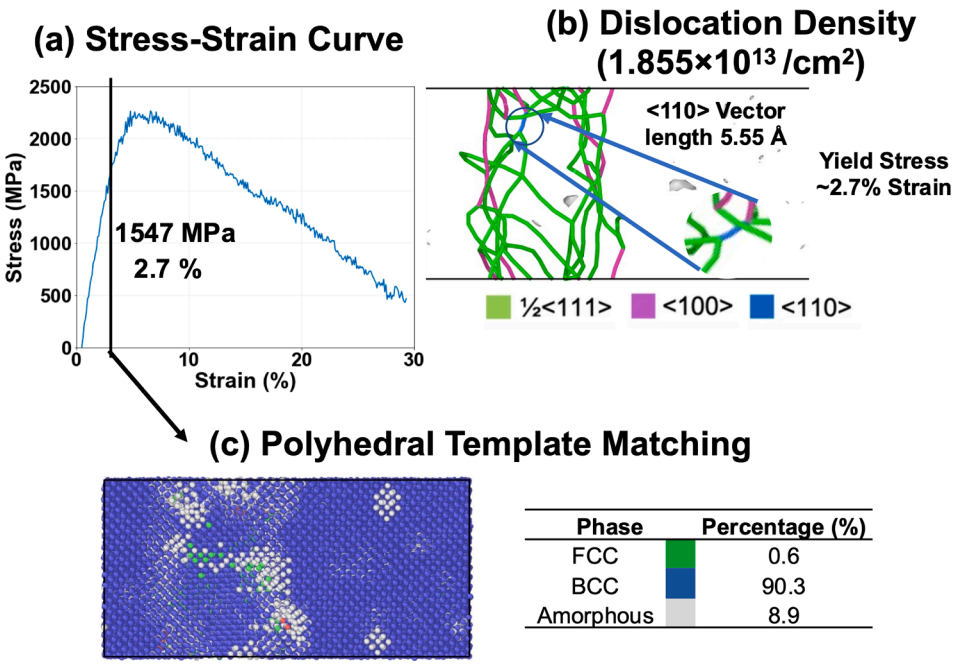

Fig. 4. The stress–strain evolution of solid-state sintered AlCoCrFeNi MPEA examined at 300 K. (a) The stress–strain curve predicts a yield stress of 1567 MPa at 2.7 % strain. (b) Dislocation analysis insinuates that the deformation is mediated by ½ ⟨1 1 1⟩ type dislocation (which is the dominant dislocation type in BCC lattices) prior to yielding, while ⟨1 1 0⟩ type dislocation is noted at the onset of yield corroborating the formation of the FCC phase. (c) Polyhedral template matching (PTM) at the yield point advocates a phase change (BCC to FCC) mediated yielding mechanism with ~ 0.6 % FCC recorded at the onset of yield.

5. Data availability

Data will be made available upon reasonable request.

CRediT authorship contribution statement

Praveen Sreeramagiri: Data curation, Formal analysis, Investigation, Methodology, Visualization. **Prince Sharma:** Investigation, Formal analysis. **Chayan Das:** Data curation, Visualization. **Ganesh Balasubramanian:** Conceptualization, Investigation, Funding acquisition, Project administration.

Declaration of Competing Interest

The authors declare that they have no known competing financial interests or personal relationships that could have appeared to influence the work reported in this paper.

Data availability

Data will be made available on request.

Acknowledgements

The simulations were performed on the Lehigh University LTS computing cluster, Hawk, acquired through the National Science Foundation (NSF) award OAC-2019035. The research was supported by the NSF award # CMMI-1944040. PS thanks the support from the University Fellowship for the P3 PhD program. Any opinions, findings, conclusions, or recommendations expressed in this material are those of the authors' and do not necessarily reflect the views of the NSF.

Appendix A. Supplementary material

Supplementary data to this article can be found online at https://doi.org/10.1016/j.commatsci.2022.111875.

References

[1] M. Kuczyk, L. Kotte, J. Kaspar, M. Zimmermann, C. Leyens, Front. Mater. 7 (2020) 242.
[2] D. Redka, C. Gadelmeier, J. Winter, M. Spellauge, C. Eulenkamp, P. Calta, U. Glatzel, J. Minár, H.P. Huber, Appl. Surf. Sci. 544 (2021), 148839.
[3] D. Johnson, R. Singh, P. Singh, A. Sharma, G. Balasubramanian, Bulletin of the Am. Phys. Soc. 65 (2020) 1.
[4] Y. Chew, G.J. Bi, Z.G. Zhu, F.L. Ng, F. Weng, S.B. Liu, S.M.L. Nai, B.Y. Lee, Mater. Sci. Eng., A 744 (2019) 137–144.
[5] C. Zhang, G.J. Chen, P.Q. Dai, Mater. Sci. Technol. (United Kingdom) 32 (2016) 1666–1672.
[6] P. Sreeramagiri, A. Bhagavatam, A. Ramakrishnan, H. Alrehaili, G.P. Dinda, J. Mater. Sci. Technol. 47 (2020) 20–28.
[7] G.P. Dinda, L. Song, J. Mazumder, Metallurgical and Mater. Trans. A 39 (2008) 2914–2922.
[8] P. Singh, V.K. Balla, A. Tofangchi, S. v. Atre, K.H. Kate, Int J Refract Metals Hard Mater 91 (2020) 105249.
[9] D. Karlsson, G. Lindwall, A. Lundbäck, M. Amnebrink, M. Boström, L. Riekehr, M. Schuisky, M. Sahlberg, U. Jansson, Addit. Manuf. 27 (2019) 72–79.
[10] Y. Zhang, J. Zhang, J. Mater. Res. 31 (2016) 2233–2243.
[11] A. Moitra, S. Kim, S.G. Kim, S.J. Park, R.M. German, M.F. Horstemeyer, Acta. Mater. 58 (2010) 3939–3951.
[12] Y. Zhang, L. Wu, H. El-Mounayri, K. Brand, J. Zhang, Procedia Manuf. 1 (2015) 296–307.
[13] B. Cheng, A.H.W. Ngan, Comput. Mater. Sci. 74 (2013) 1–11.
[14] J. Xu, R. Sakanoi, Y. Higuchi, N. Ozawa, K. Sato, T. Hashida, M. Kubo, J. Phys. Chem. C 117 (2013) 9663–9672.
[15] B. Cheng, A.H.W. Ngan, Int. J. Plast. 47 (2013) 65–79.
[16] A.G. Elliot, Z.A. Munir, Journal of Materials Science 1968 3:2 3 (1968) 150–157.
[17] R.M. German, Z.A. Munir, J. Am. Ceram. Soc. 59 (1976) 379–383.
[18] A. Fourmont, S. le Gallet, O. Politano, C. Desgranges, F. Baras, J. Alloy. Compd. 820 (2020), 153448.
[19] D. Farkas, A. Caro, J. Mater. Res. 35 (2020) 3031–3040.
[20] P. Sreeramagiri, G. Balasubramanian, Additive Manuf. Lett. 3 (2022), 100045.
[21] P. Sreeramagiri, A. Roy, G. Balasubramanian, J. Phase Equilibria. Diffus 42 (2021) 772–780.
[22] A. Roy, P. Sreeramagiri, T. Babuska, B. Krick, P.K. Ray, G. Balasubramanian, Mater. Charact. 172 (2021), 110877.
[23] X.W. Zhou, R.A. Johnson, H.N.G. Wadley, Phys. Rev. B 69 (2004), 144113.
[24] Z. Lin, R.A. Johnson, L. v Zhigilei, Phys Rev B 77 (2008) 21410.
[25] A. Sharma, P. Singh, D.D. Johnson, P.K. Liaw, G. Balasubramanian, Sci. Rep. 6 (2016) 31028.
[26] A. Sharma, S.A. Deshmukh, P.K. Liaw, G. Balasubramanian, Scr. Mater. 141 (2017) 54–57.
[27] P. Sreeramagiri, H. Alrehaili, X. Wu, G. Dinda, G. Balasubramanian, J. Mater. Res. Technol. 19 (2022) 1090–1101.
[28] S. Plimpton, J. Comput. Phys. 117 (1995) 1–19.
[29] A. Stukowski, Model Simul. Mat. Sci. Eng. 18 (2009), 015012.
[30] W.D. Callister Jr, D.G. Rethwisch, Materials Science and Engineering - An Introduction 10th Edition, 2018.
[31] P.M. Larsen, Sø. Schmidt, J. SchiØtz, Model Simul Mat Sci Eng 24 (2016) 055007.

[32] H. Pan, S.H. Ko, C.P. Grigoropoulos, J. Heat Transfer 130 (2008).
[33] R.M. German, Sintering of Adv. Mater. (2010) 3–32.
[34] R. German, Sintering: From Empirical Observations to Scientific Principles, Elsevier Inc., 2014.
[35] R.M. German, JOM 68 (2016) 878–884.
[36] A. Roy, J. Munshi, G. Balasubramanian, Intermetallics (Barking) 131 (2021), 107106.
[37] D. Lazarus, in: Materials Research Society Symposia Proceedings, Materials Research Soc, 1987, pp. 297–311.
[38] A. Roy, R. Devanathan, D.D. Johnson, G. Balasubramanian, Mater. Chem. Phys. 277 (2022), 125546.